NANO MICRO
small

Supporting Information

for *Small,* DOI: 10.1002/smll.201700543

Efficiency of Cathodoluminescence Emission by Nitrogen-Vacancy Color Centers in Nanodiamonds

*Huiliang Zhang, David R. Glenn, Richard Schalek, Jeff W. Lichtman, and Ronald L. Walsworth**

Supporting Information

Efficiency of Cathodoluminescence Emission by Nitrogen-Vacancy Color Centers in Nanodiamond

*Huiliang Zhang, David R. Glenn, Richard Schalek, Jeff W. Lichtman, Ronald L. Walsworth**

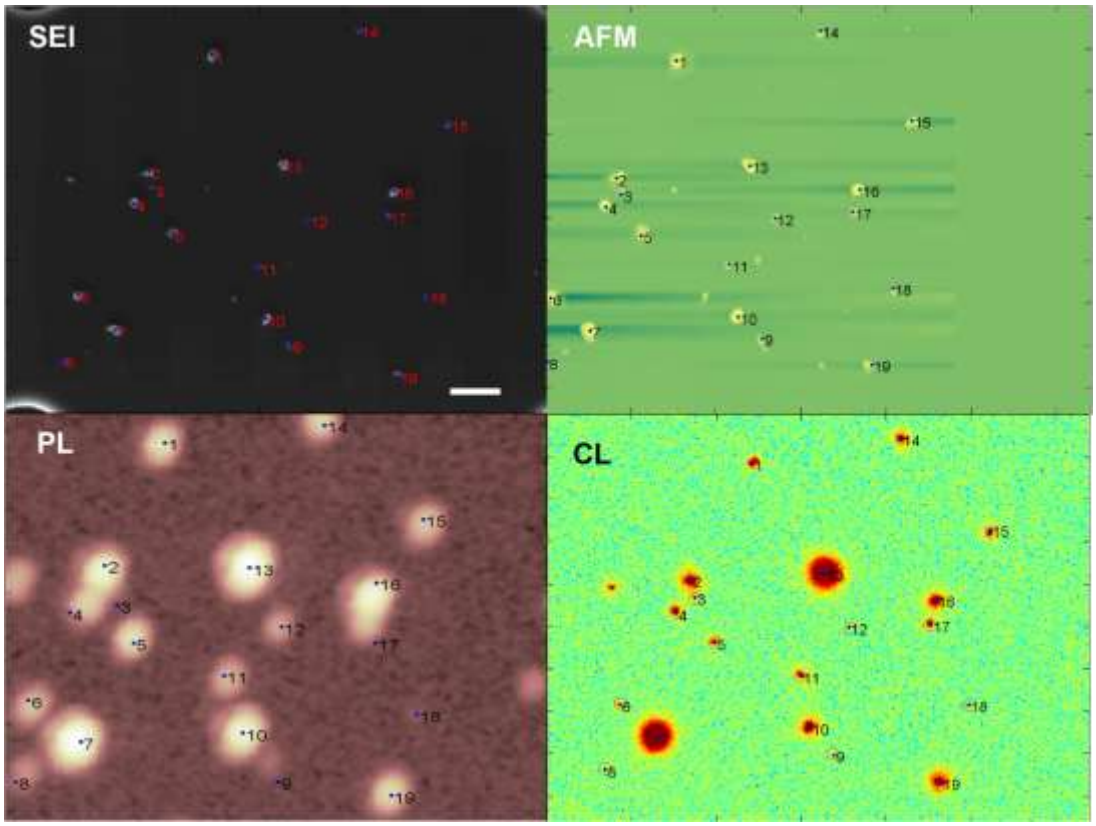

Figure S1. Typical co-registered nanodiamond (ND) images. All NDs in our data set were successively imaged using secondary electron (SEI) microscopy, atomic force microscopy (AFM), photo-luminescence (PL) microscopy, and cathodoluminescence (CL). The NDs were deposited onto silicon wafers etched with a numbered grid to facilitate registration of fields of view obtained in different instruments. (The edges of features demarcating one grid location are visible in the corners of the SEI image here.) Image registration was carried out using custom *Matlab* software, and only NDs with visible and non-saturated images in all four instruments were included in the full data set. NDs that were imaged in SEI, AFM, and PL, but had no detectable CL signal, were also included in the data used to generate Figures 1 and 3 of the main text, but were excluded from Figure 4. In the images above, 17 of the 19 numbered NDs were visible in all four images, while two (labeled 9 and 18) were not detectable in CL. The total data set consisted of n = 257 co-registered NDs, obtained from 20 sets of images. Of these, $n_{CL>0}$ = 195 had CL signals distinguishable from background. Scale bar 1 µm.

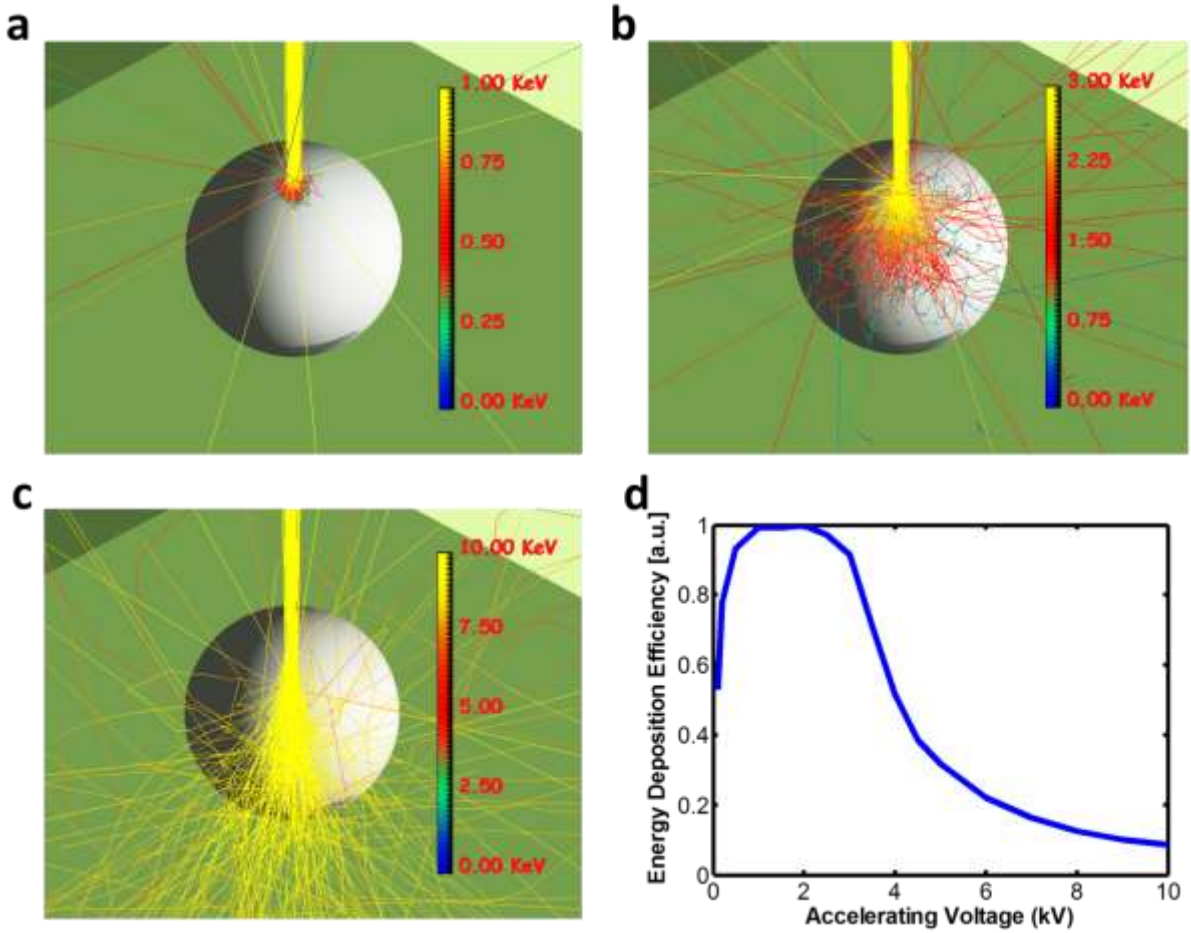

Figure S2: Simulation of injected e-beam scattering trajectories**.** To estimate the efficiency of energy deposition by electrons impinging on nanodiamonds (NDs) of various sizes, we carried out a series of numerical simulations using the CASINO software package. (CASINO = monte CArlo SImulation of electroN trajectory in sOlids). To illustrate the qualitative behavior of electron trajectories at various energies,we show calculations carried out for spherical diamond nanoparticles of diameter d = 100 nm, at the following energies: (**a)** 1 keV (**b)** 3 keV, (**c)** 10 keV . The color of the electron trajectories in each figure indicates the energy of a particular electron in the calculated ensemble. Electrons undergo continuous energy loss by inelastic scattering, punctuated by random elastic scattering events which result in sudden changes in energy and momentum. In these simulations, slow (1 keV) electrons are completely stopped within the first ~10 nm of the particle, whereas fast (10 keV) electrons travel ballistically through the whole ND while depositing only a small fraction of their energy. (**d**) Energy deposition efficiency (ratio of deposited energy to total incident electron energy) as a function of accelerating voltage. For the 100 nm diameter particles, optimized energy deposition efficiency can be achieved for accelerating voltages of about 1 - 3 kV.

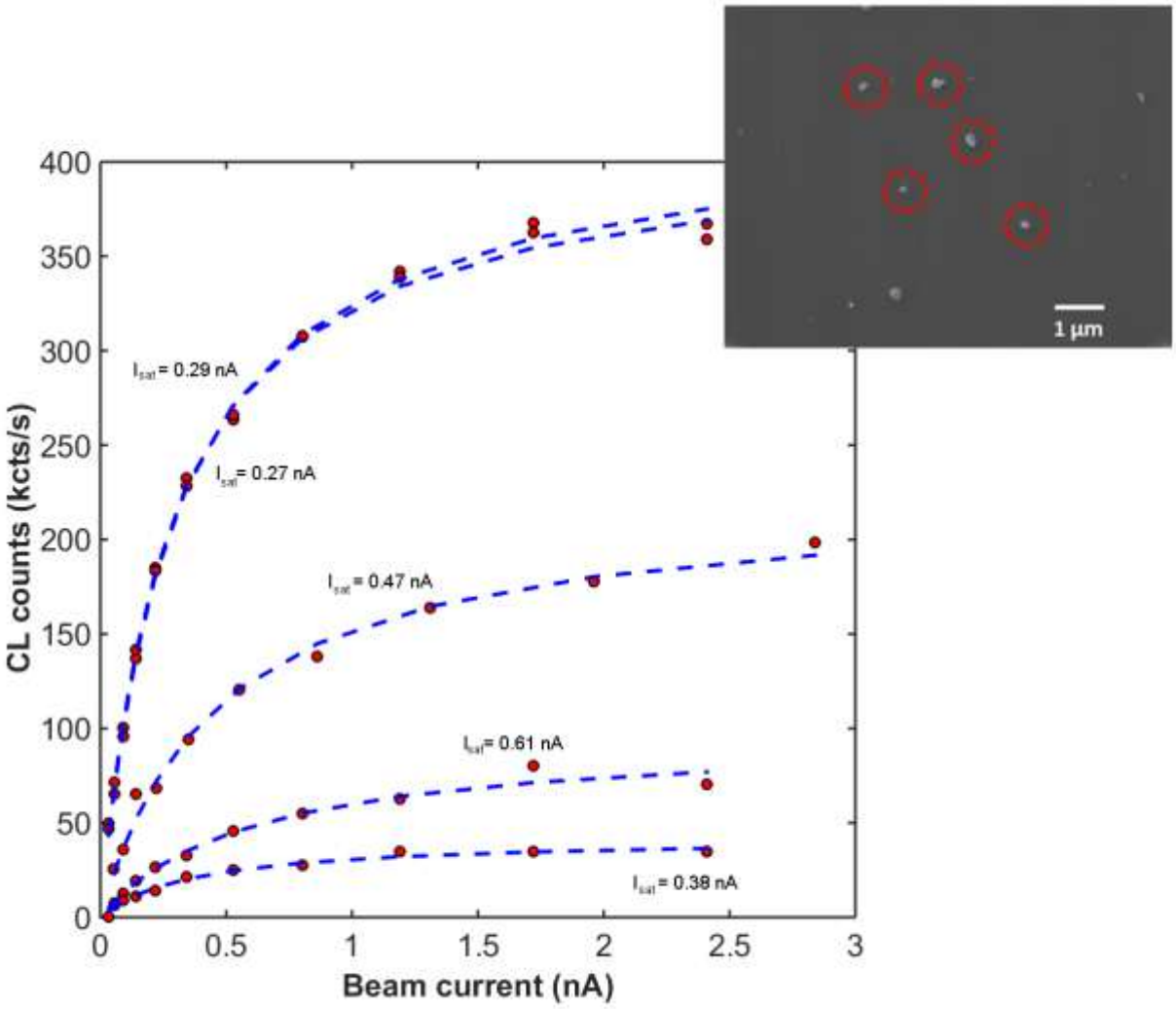

Figure S3. Characterization of CL intensity saturation with e-beam current. Inset SEM image shows five typical nanodiamonds (NDs) from our sample. For each of these NDs, we measured the dependence of CL intensity on e-beam current at fixed accelerating voltage V = 5 keV. The detected CL intensity saturates at large currents, as the rate of electron-hole-pair (EHP) generation and conversion to nitrogen-vacancy (NV) electronic excitations approaches the NV excited-state lifetime. The observed saturation behavior may also be due in part to charging effects at the sample surface. Typical saturation currents for NDs in our sample were on the order of $I_{sat} \approx 0.3 - 0.5$ nA, obtained by fitting CL data to the following form:

$$S_{CL} = \frac{S_{max}\left(\frac{I}{I_{sat}}\right)}{1+\left(\frac{I}{I_{sat}}\right)}.$$

We performed all CL measurements described in the main text at a current I = 1 nA, well above I_{sat}, to ensure that variations in the detected CL rates were primarily due to NV density and/or surface quenching-related effects, rather than e-beam-limited EHP generation rates. Higher operating currents could not easily be used due to sample charging issues.

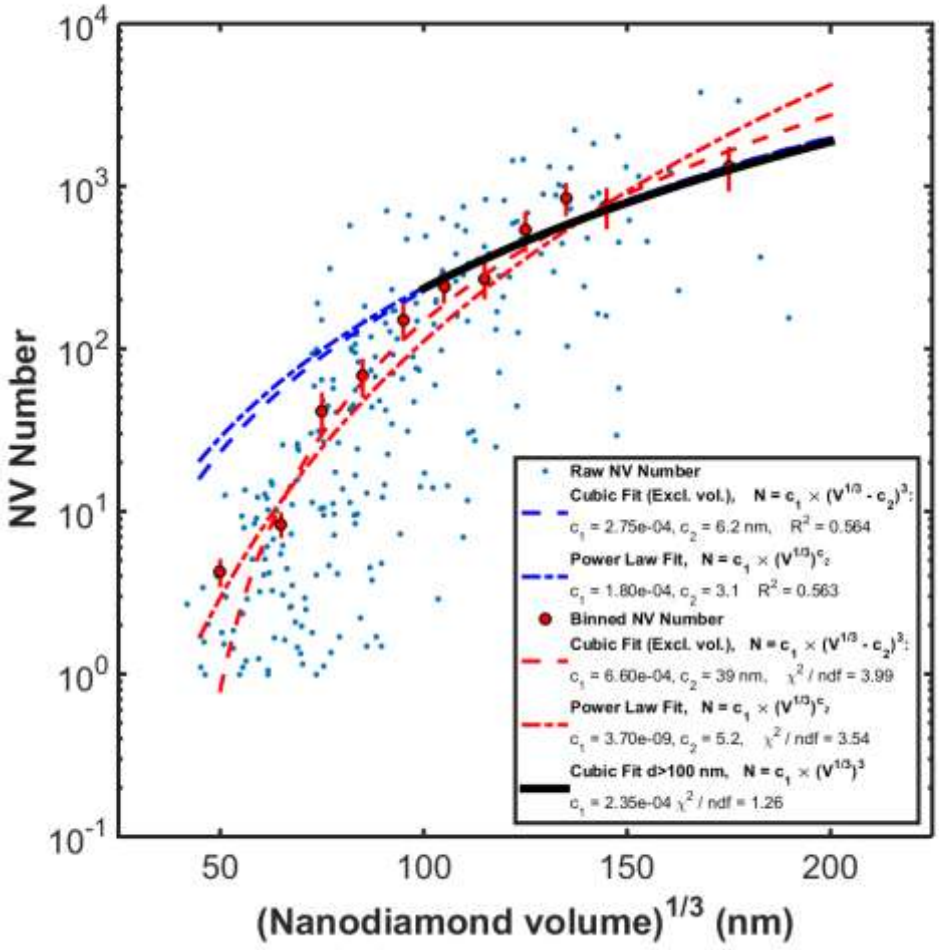

Figure S4: Comparison of models for nitrogen-vacancy (NV) defect number vs. nanodiamond (ND) size. Blue dots show estimated number of NV centers per ND (obtained from photoluminescence measurements) as a function of ND size (obtained from secondary electron imaging and atomic force microscopy). ND size is parameterized as the cube-root of the measured ND volume, $d = V^{1/3} = (w_x \cdot w_y \cdot h)^{1/3}$. Red circles show the same data, with NVs binned by size in 10 nm intervals. Error bars are the standard error in the mean of each bin, $\sigma/n^{1/2}$. Fits were made to two different models to investigate dependence of NV number on ND size, including (i) a simple power law $N = (c_1 \cdot V^{1/3})^{c2}$, and (ii) an excluded volume model, $N = c_1 \cdot (V^{1/3} - c_2)^3$. The power law should yield a d^3 dependence in the simplest case of constant NV density. The excluded volume model *assumes* this cubic dependence, but allows for a depleted surface layer of variable thickness, in which NVs are unable to form or have suppressed photoluminescence due to surface quenching. Dashed and dotted blue lines show equal-weighted least squares fits of the un-binned data to each model. The fits are dominated by population of NDs with large d, demonstrating the need for binning and appropriate weighting for correct analysis of the data. Dashed and dotted red lines show fits of the binned data to the cubic excluded volume model and the power law model, respectively. Fits on the full data set are consistent with neither model; in both cases, χ^2 / n.d.f. > 3. However, if only the large-volume NDs are included, d > 100 nm, then the binned data are consistent with a fit to a simple cubic, $N = c_1 \cdot d^3$ (solid black line). Because the anomalously low NV numbers for small NDs are apparently not consistent with the excluded volume model, we attribute the deviation from constant density to a size-dependent decrease in NV creation efficiency during sample preparation. Finally, we note that the binned data are analyzed here using only the

statistical uncertainty $\sigma/n^{1/2}$, rather than the more conservative $\sigma_{Tot} = (\sigma_{inst}^2 + \sigma/n)^{1/2}$used in the main text. If we repeat the analysis here, including the large instrumental uncertainty estimated from the photoluminescence calibration, we obtain χ^2/ndf = 1.3 for the cubic excluded volume fit, χ^2/ndf = 1.4 for the power law, and χ^2/ndf = 0.53 for the cubic fit at d > 100 nm. In this case, all models would apparently consistent with the data. However, we believe that this uncertainty estimate is in fact too conservative, given the very low χ^2 that results for the cubic fit to large NDs. A more precise account of the PL calibration uncertainty (and significantly more PL calibration data, ideally including single-NV-containing NDs over the full 20 nm– 200 nm size range of our main sample) would be needed to fully resolve this question.

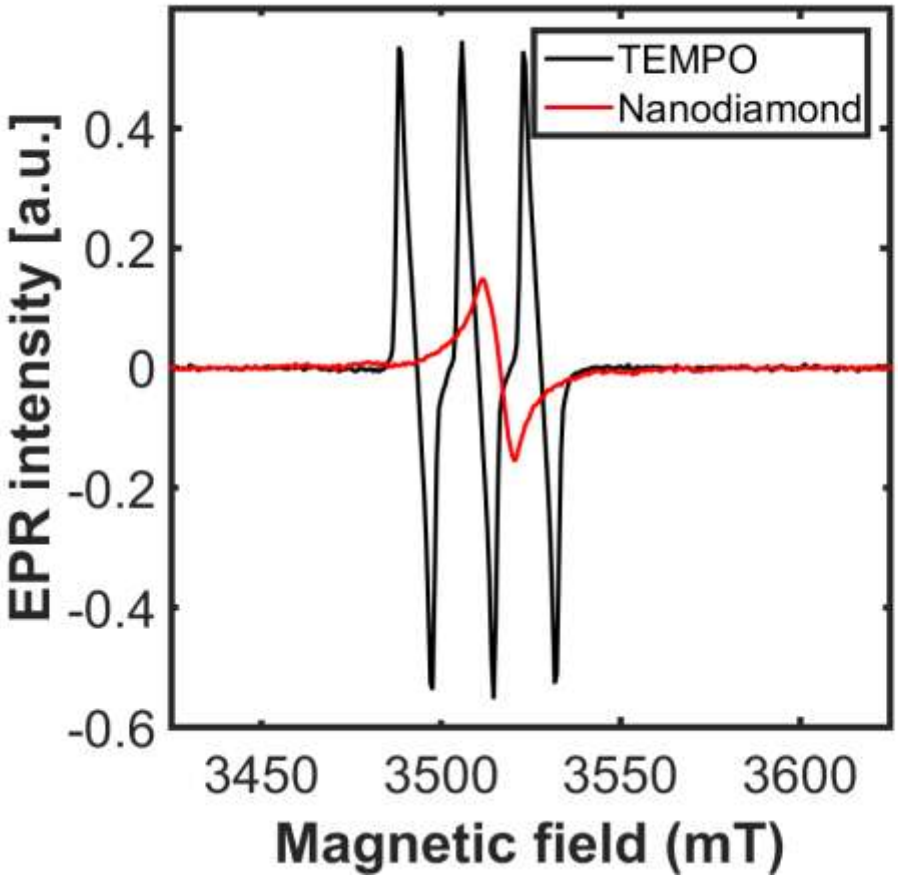

Figure S5. Background-subtracted EPR spectra: TEMPO calibration standard (black trace), and our primary, red-CL emitting, He^{+}-irradiated HPHT nanodiamond sample (red trace). To estimate the electronic spin density in each sample, we integrated each spectrum twice (since EPR spectra as shown are the derivative of microwave absorption spectra). The relative doubly-integrated signals were approximately 103 (TEMPO) : 69 (HPHT ND). The TEMPO solution was 50 µL in volume and had a concentration of 20 µM; the nanodiamond solution was 35 µL in volume, prepared at a concentration of 1 mg / ml. We therefore estimate the paramagnetic (nitrogen) spin concentration in the diamond sample ~230 ppm. This concentration is approximately consistent with reported values in the literature for nanodiamonds with moderately high paramagnetic nitrogen content.[38]